

A novel stress isolation guard-ring design for the improvement of a three-axis piezoresistive accelerometer

This article has been downloaded from IOPscience. Please scroll down to see the full text article.

2011 J. Micromech. Microeng. 21 105006

(<http://iopscience.iop.org/0960-1317/21/10/105006>)

View [the table of contents for this issue](#), or go to the [journal homepage](#) for more

Download details:

IP Address: 140.114.56.248

The article was downloaded on 09/03/2012 at 02:13

Please note that [terms and conditions apply](#).

A novel stress isolation guard-ring design for the improvement of a three-axis piezoresistive accelerometer

Hsieh-Shen Hsieh¹, Heng-Chung Chang^{1,3}, Chih-Fan Hu¹,
Chao-Lin Cheng¹ and Weileun Fang^{1,2}

¹ Power Mechanical Engineering Department, National Tsing Hua University, Hsinchu, Taiwan

² NEMS Institute, National Tsing Hua University, Hsinchu, Taiwan

³ MEMS/MST R&D Department, Research Center, Delta Electronics, Inc., Taoyuan, Taiwan

E-mail: fang@pme.nthu.edu.tw

Received 18 May 2011, in final form 25 July 2011

Published 7 September 2011

Online at stacks.iop.org/JMM/21/105006

Abstract

This study designs and implements a stress isolation guard-ring structure to improve the performances of the existing single proof-mass three-axis piezoresistive accelerometer. Thus, the environment disturbances, such as temperature variation and force/deflection transmittance, for a packaged three-axis piezoresistive accelerometer are significantly reduced. In application, the three-axis piezoresistive accelerometer has been fabricated using the bulk micromachining process on the SOI wafer. Experimental results show that the out-of-plane deformation of the suspended spring mass on the packaged accelerometer is reduced from 0.72 to 0.10 μm at a 150 °C temperature elevation. The temperature coefficient of zero-*g* offset for the presented sensor is reduced, and the temperature-induced sensitivity variation is minimized as well. Measurements also demonstrate that the guard-ring design successfully reduces the false signals induced by the force and displacement transmittance disturbances for one order of magnitude. Moreover, the three-axis acceleration sensing for the presented accelerometer with guard ring has also been demonstrated with sensitivities of 0.12–0.17 $\text{mV V}^{-1} \text{g}^{-1}$ and nonlinearity < 1.02%.

(Some figures in this article are in colour only in the electronic version)

1. Introduction

The silicon-based MEMS (micro-electro mechanical system) accelerometers with small size, batch process and capability of integrating with sensing circuits play an important role in motion sensing applications. In general, the MEMS accelerometer consists of suspended spring and mass structures. These suspended mechanical structures could have unwanted deformation and displacement resulting from the stresses induced by the packaging [1–7]. For instance, the accelerometer chip is fixed to a base using adhesives [3–6]. The suspended MEMS structures are subjected to a load induced by the thermal mismatch among the silicon substrate, adhesive and base after the high-temperature curing process [4–6]. Similarly, temperature fluctuation will also introduce a load to spring–mass structures of the packaged accelerometer

[2, 7]. In summary, the performance of the MEMS accelerometer is frequently influenced after packaging. Thus, in addition to electrical connections, stress isolation is also a critical concern for the packaging of the MEMS accelerometer [1–3].

Recently, various approaches have been reported to reduce the packaging-induced stress problem [3, 8–13]. The soft silicone coating on a MEMS sensor with cap bonding and the four-dot die-attach process is used in [3] to lower the packaging stress. In addition, a bonding material with a coefficient of thermal expansion (CTE) close to silicon is employed in [8, 9] to reduce the unwanted stress of a capacitive pressure sensor induced by bonding. However, since the boundary of the suspended MEMS structure is fixed after packaging, a certain level of stress is still transferred to the sensors due to the relative displacement of the anchors.

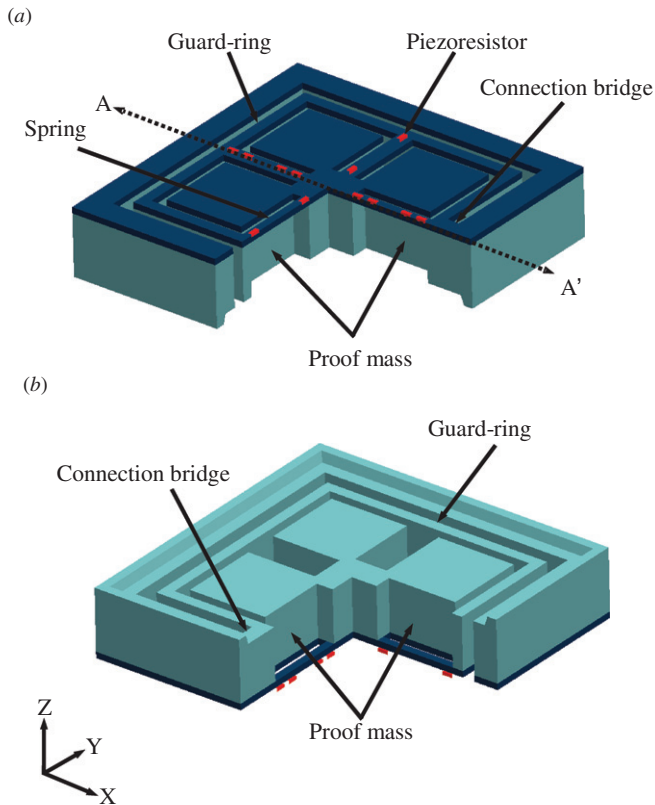


Figure 1. Schematic illustrations of the present three-axis accelerometer with guard-ring design: (a) the front-side view of the piezoresistive accelerometer formed by the SOI wafer and (b) the backside view of the accelerometer.

The design of surrounding proof mass is exploited in [10] to reduce the influence of thermal residual stress on the three-axis piezoresistive accelerometer for a high-temperature range application. In this case, an additional bonding process is required to provide mechanical support for chip handling. Moreover, since the anchor is in the center of the chip, special wire bonding (for signal connection) and package structure are required. The twin-mass piezoresistive accelerometer with Quad beam design to reduce the package stress is reported in [11]. A novel membrane structure design to reduce the package stress for MEMS pressure sensors is also investigated [12, 13]. However, a certain amount of the packaging-induced stress could still transfer to the sensor by the flexure structure.

Therefore, this study presents the design of a novel stress isolation guard-ring structure to reduce the unwanted spring deflection as well as the output signals induced by the environmental disturbances for a packaged accelerometer [14]. Thus, the performances of the packaged piezoresistive accelerometer are improved. In application, the guard-ring structure is successfully implemented on the existing single proof-mass three-axis piezoresistive accelerometer [15–18]. Measurements demonstrate that the influence of environment disturbances is significantly suppressed by the guard-ring design, yet the characteristic of three-axis sensing remains unchanged.

2. Sensor design

This study designs and implements a three-axis piezoresistive accelerometer with stress isolation guard-ring structure on a SOI wafer. The schematic illustration in figure 1(a) shows the front-side view of the proposed three-axis accelerometer formed by the device layer of a SOI wafer. In addition, figure 1(b) shows the backside view of the accelerometer formed by the handle silicon layer of a SOI wafer. The proposed accelerometer design consists of a central proof mass, four springs, a stress isolation guard ring and 12 piezoresistors. The piezoresistors are formed by the doped silicon on the surface of springs. The springs made of the device silicon layer of the SOI wafer are used to support the proof mass. Moreover, the springs are fixed to the suspended guard ring. As indicated in figures 1(a) and (b), the guard ring is anchored to the substrate through the connection bridge only at one end. Table 1 depicts the typical dimensions of various parts of the presented accelerometer design.

As a comparison, figures 2(a) and (b) show the existing and proposed accelerometer designs, respectively. As shown in figure 2(a), the spring mass of the existing accelerometer is directly anchored to the substrate. Thus, any relative distance change between two anchors (induced by temperature variation, force, etc) will lead to spring deformation. The change in resistance of piezoresistors is induced, and then it causes the sensor to produce an unwanted signal output. As indicated in figure 2(b), the spring mass of the proposed design is fixed to the surrounding guard ring. Since the guard ring is only anchored to the substrate at one end, the structure deformation due to temperature variation and substrate loading can be released from the free end. Thus, the unwanted spring deformation and signal output can be reduced. Therefore, the proposed design can protect such a packaged three-axis accelerometer from environment disturbances. To show the design concept, commercial finite element software (ANSYS) was used to predict the mechanical behavior of the sensor chip adhered to a base. The typical simulation results in figure 2(c) show the deformation of spring–mass structures under the thermal loading (by temperature variation). It indicates that the springs of the accelerometer without the guard ring will be deformed by the thermal load, whereas the springs of the proposed accelerometer design have only angular displacement with the guard ring after applying the thermal load. In addition, the guard-ring structure and connection bridge are designed to be much stiffer than the springs of the accelerometer. According to the FEM simulations presented in table 2, the guard-ring structure has much smaller displacement in comparison to the spring mass of the accelerometer for the first three vibration modes. Thus, the guard ring and connection bridge during operation can be considered as a rigid body. As a result, the influence of the guard ring on the dynamic characteristics of the accelerometer can be ignored.

As shown in figure 3(a), the three-axis accelerations cause different bending and twisting deformations of springs and can be detected by different resistance changes in piezoresistors. According to the concept presented in

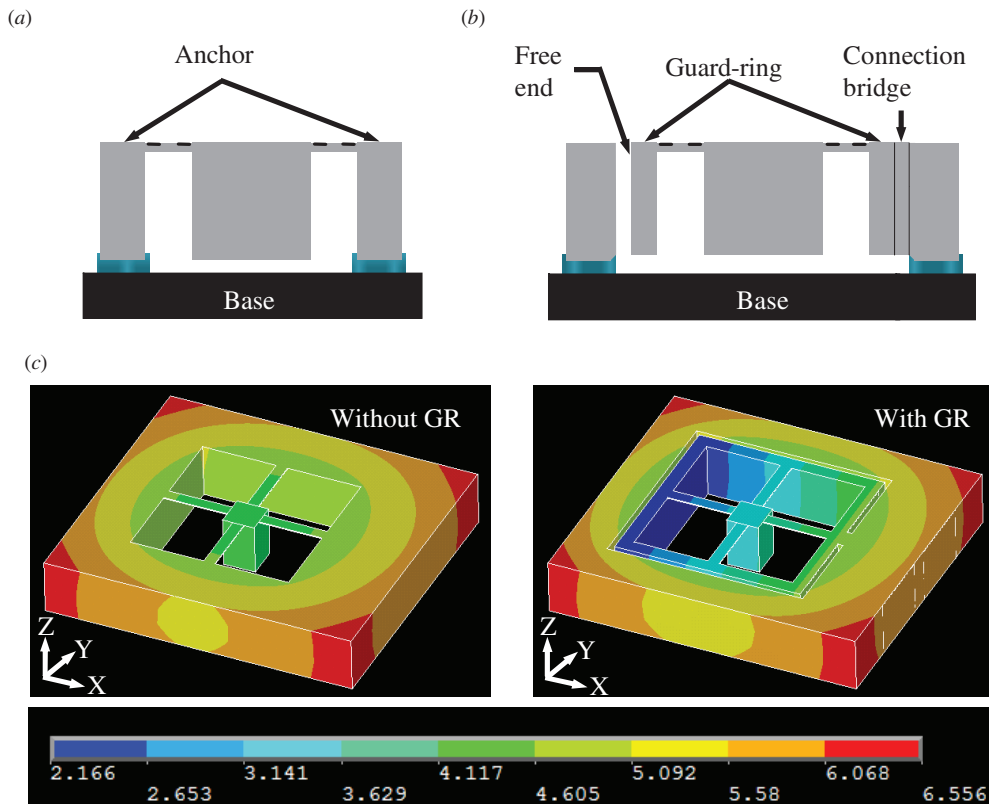


Figure 2. Schematic illustrations of the cross-sectional views of the existing and proposed accelerometer (the AA' cross sections indicated in figure 1): (a) the existing accelerometer design. The springs are directly anchored to the substrate. (b) The proposed accelerometer design. The springs are anchored to the guard ring. (c) The deformation distribution FEA results of the sensors under the external thermal loading applied (GR: guard ring).

Table 1. The typical dimensions of various parts of the presented accelerometer design.

Spring	Connection beam	Guard-ring	Proof-mass

Unit: μm

[15–18], the piezoresistors embedded in the springs of the proposed accelerometer can be exploited to measure the accelerations of three different axes. The distribution of piezoresistors in the springs is shown in figure 3(b). The resistivity of the piezoresistors is changed as the springs experience bending or twisting deformations induced by the accelerations. Figure 3(c) further shows the schematic

illuminations of the accelerometer structure displacement plots for the three-axis accelerations and the associated variation on Wheatstone bridges. The blue and red arrows represent the increase and decrease of resistances, respectively. Moreover, the piezoresistors on the surface of the (100) Si wafer are aligned with the $\langle 110 \rangle$ axes of the Si crystal. Thus, the piezoresistors have no resistance change as the spring is

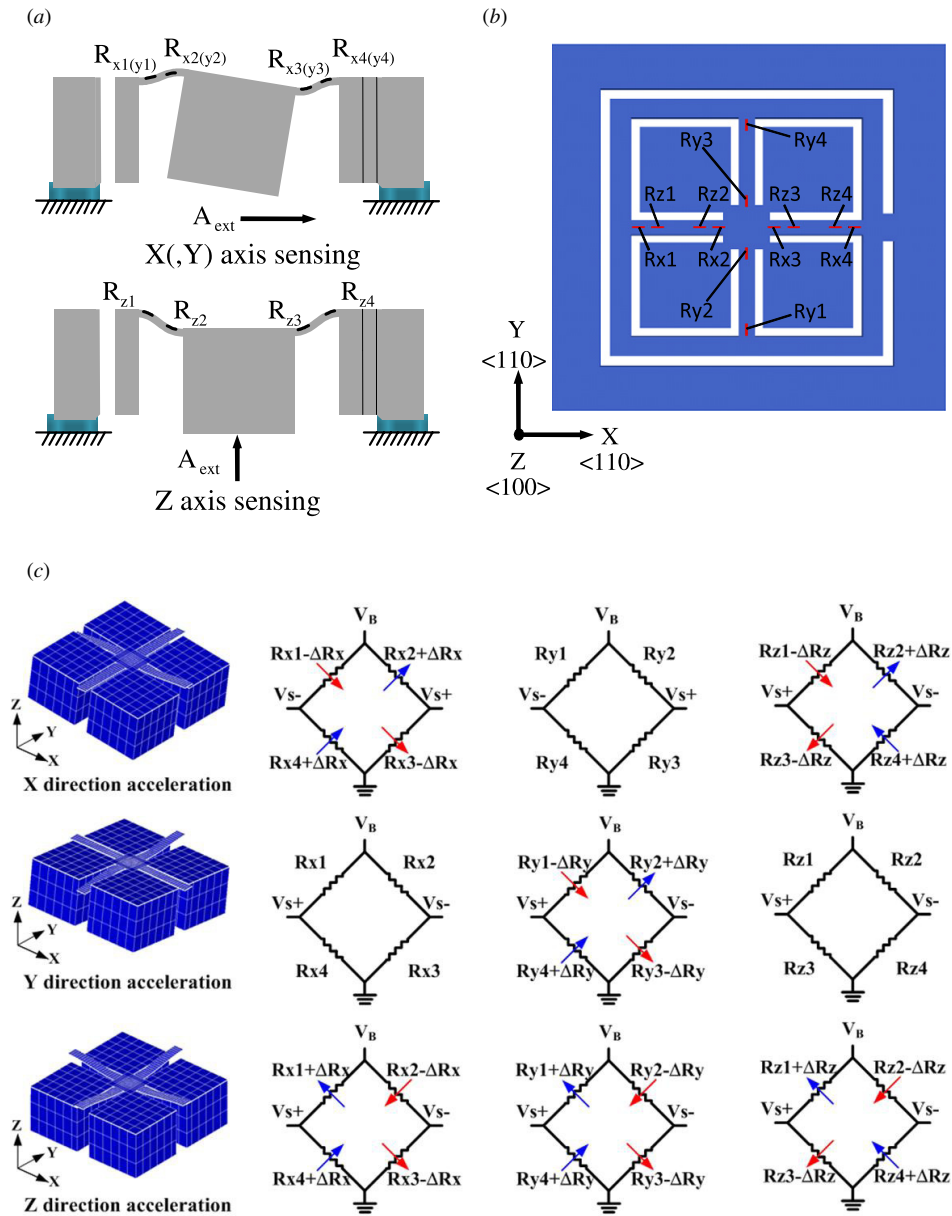
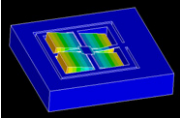
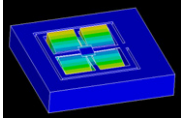
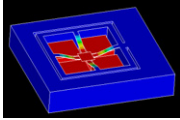


Figure 3. (a) The operation principle of the proposed single proof-mass three-axis accelerometer in different axes, (b) arrangement layout of piezoresistors on the beams, (c) schematic illustration of the accelerometer structure displacement plots for the three perpendicular accelerations and their effects on the x, y and z Wheatstone bridges. The blue arrows show resistance increase and the red arrows show resistance decrease.

Table 2. The predicted and measured first three vibration modes of the proposed accelerometer.

	Mode I Y-rotation	Mode II X-rotation	Mode III Z-translation
Mode Shape			
FEA Results (kHz)	1.42	1.42	1.94
Experimental Results (kHz)	1.57	1.59	2.33
Difference (%)	-9.55	-10.69	-16.74

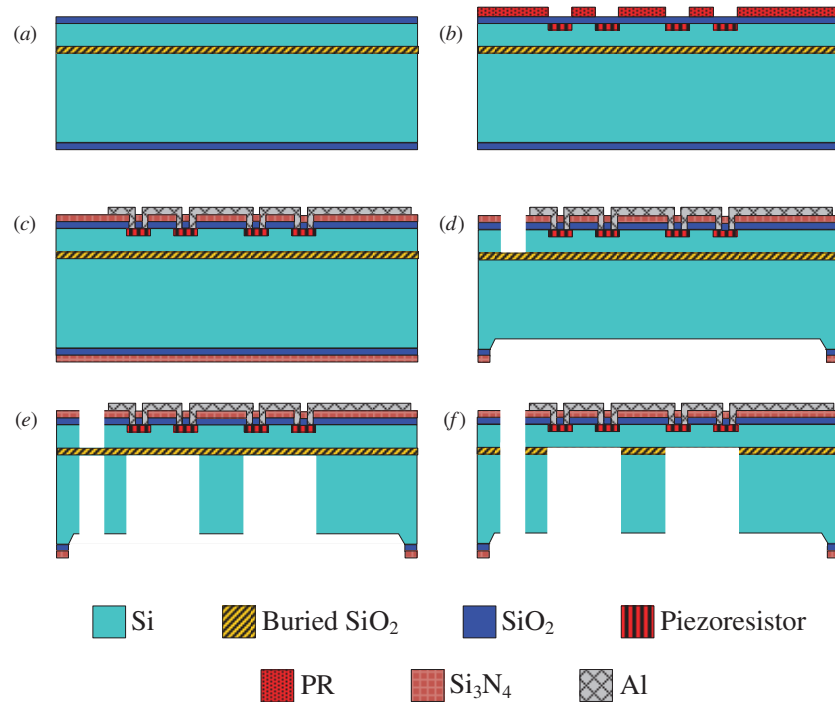


Figure 4. The fabrication process steps at the AA' cross section depicted in figure 1(a). (a) Deposit insulator, (b) diffuse piezoresistors, (c) deposit and pattern metal, (d) patterned front-side DRIE Si and backside wet etching Si, (e) DRIE backside Si and (f) structure release.

subjected to a torsional deformation. The unwanted cross-axis sensitivity can be minimized via circuit configurations and mechanical design [15–18].

3. Fabrication process

The fabrication process steps (seven photo masks) to implement the proposed devices are shown in figure 4. As shown in figure 4(a), the process was performed on a 4-inch n-type (100) SOI wafer with a 6.5 μm thick device silicon layer on a 400 μm thick handle substrate, and the thickness of the buried silicon oxide was 1 μm . The processes began with the growth of 40 nm thermal oxide (as the screen oxide), and then the first two photo masks were used to define the patterns of the piezoresistors and the heavily doped silicon electrical routing. The piezoresistors were aligned with the $\langle 110 \rangle$ crystal directions. Boron ions were implanted to form the p-type piezoresistors strips using the ion implanter, as shown in figure 4(b). After that, the thermal annealing process was employed for the damage recovery of the crystalline silicon and then the screen oxide was removed. As shown in figure 4(c), 100 nm thermal oxide and 170 nm LPCVD (low-pressure chemical vapor deposition) silicon nitride films were deposited and patterned to define the contact window for heavily doped silicon. The aluminum metal film which acted as the electrical link was deposited by a physical vapor deposition system and patterned by reactive ion etching. A 30 min annealing process at 410 $^{\circ}\text{C}$ was performed to ensure ohmic contact between metal and semiconductor layers. As shown in figure 4(d), the first deep reactive ion etching (DRIE) process was used to define the patterns of the central mass, spring, guard ring and connection bridge on the device silicon

layer of the SOI wafer. After that, the silicon nitride and oxide films on the backside of the SOI wafer were patterned for the following silicon wet etching. The SOI wafer with front side protected by a mechanical holder was immersed into a potassium hydroxide (KOH) solution to etch a 20 μm cavity on the backside substrate surface. The cavity indicated in figure 4(d) offers space for the moveable parts of the sensor. As shown in figure 4(e), after the backside of the SOI wafer was covered with a 10 μm thick patterned photoresist, the second DRIE process was employed to define the dimensions of the central proof mass, guard ring and connection bridge on the handling silicon layer of the SOI wafer. The thick photoresist was removed after the DRIE. Finally, the wafer was immersed into a buffer oxide etch solution to remove the buried oxide layer of the SOI wafer to release the structures, as shown in figure 4(f).

Figure 5 shows the typical fabrication results of the proposed accelerometer. The scanning electron microscopy micrographs in figures 5(a) and (b) display the front-side and backside view of the accelerometer, respectively. The thin spring (device silicon layer only), and thick proof mass, guard ring and connection bridge (device and handling silicon layers) are clearly observed. The mass is connected to the guard ring through the springs. The connection bridge between the guard ring and the substrate is also observed. The zoom-in micrograph in figure 5(c) shows the heavily doped Si on the spring of the piezoresistor and the related metal electrical routings on the spring and guard ring. The zoom-in micrographs in figures 5(d) and (e) further show the front side and backside of the connection bridge. The signal routings distributed on the front side of the connection bridge are clearly observed. The photograph in figure 5(f) shows

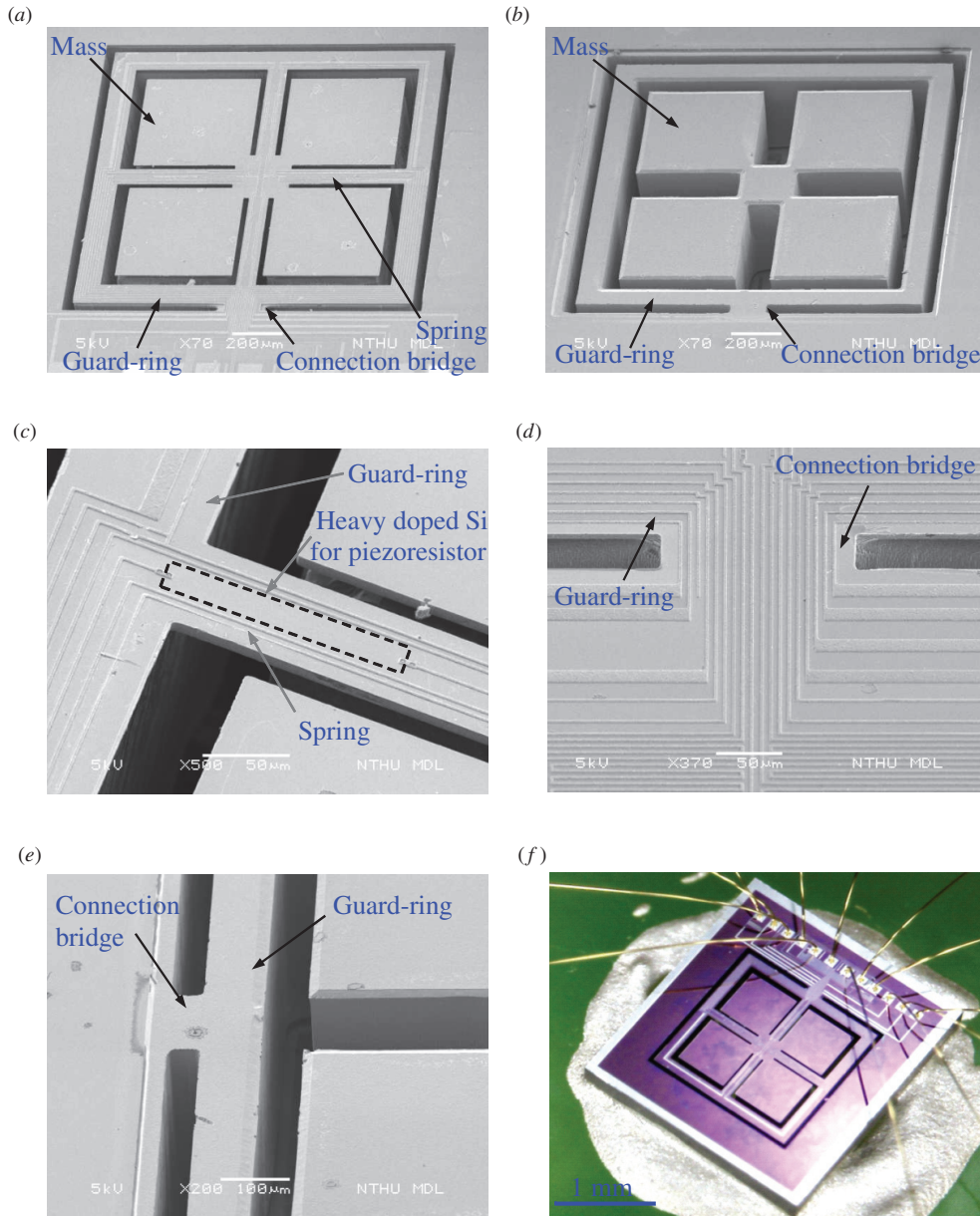


Figure 5. Micrographs of the fabricated proposed accelerometer: (a) the front-side view, (b) the backside view, (c) the zoom-in micrograph of the heavily doped Si on spring for the piezoresistor and the related metal electrical routings on the spring and guard ring, (d), (e) the zoom-in micrographs of the front side and backside of the connection bridge and (f) after wire bonding.

the accelerometer mounted on a printed circuit board (PCB) after wire bonding. The size of this three-axis piezoresistive accelerometer chip is 2.3 mm × 2.1 mm.

4. Results and discussions

This study has performed various tests to characterize the performance of the fabricated three-axis accelerometer. First, the frequency response and the vibration mode shape were measured by the Micro Motion Analyzer (commercial product offered by Polytec GmbH, Germany). Measurement results in figure 6 show the first four resonant frequencies. The associated vibration mode shapes predicted from the simulation are listed in table 2. In summary, the first vibration

mode (*Y*-rotation) at 1.57 kHz is for *X*-axis acceleration sensing. The second vibration mode (*X*-rotation) at 1.59 kHz is for *Y*-axis acceleration sensing. The third vibration mode (*Z*-translation) at 2.33 kHz is for *Z*-axis acceleration sensing. Moreover, the fourth vibration mode is 16.82 kHz, which indicates that the unwanted higher modes are far from the first three modes. Therefore, the performance of the proposed three-axis accelerometer with guard-ring design has less influence on the dynamics of spring–mass and guard-ring structures. Table 2 also lists the resonant frequencies predicted from the simulation as a comparison. The deviation between the prediction and measurement is mainly caused by the difference of the spring shape between the simulation model and the fabrication one. Other tests are discussed as follows.

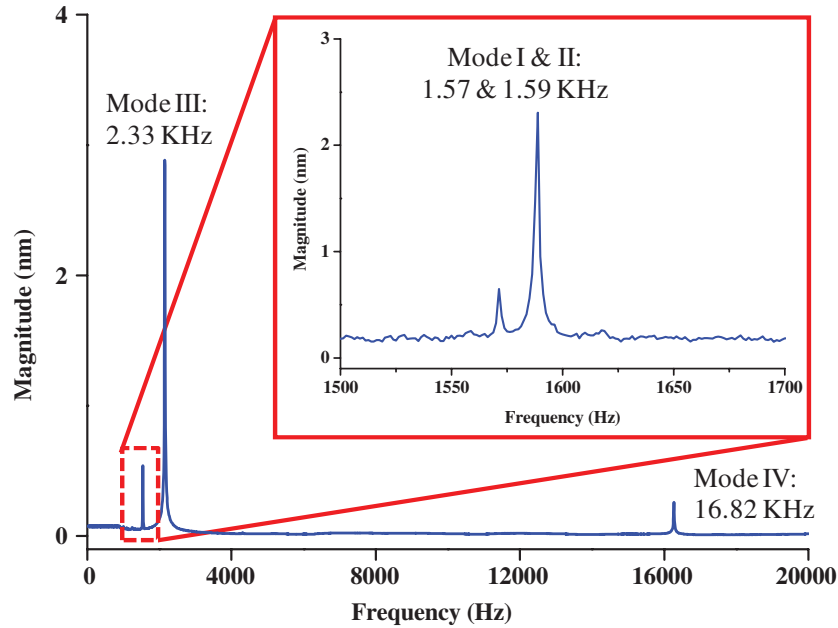


Figure 6. The modes measured by the MMA-300 Micro System Analyzer; modes I, II, pitch/roll modes for X-, Y-axis sensing; mode III, out-of-plane translation mode for Z-axis sensing. Simulations agree well with measurements.

4.1. Spring–mass deformation by temperature variation tests

Figure 7(a) shows the experimental apparatus to characterize the out-of-plane deformation of the spring–mass structure induced by the ambient temperature change. The packaged accelerometer chip with a handling silicon layer adhered to the PCB was heated by the hot plate. The heating temperature was modulated by a controller. As predicted in figure 2(c), the springs of the accelerometer will be deformed by thermal load due to the mismatch of thermal expansion coefficients among the silicon substrate, PCB and adhesives. As a result, the spring–mass structure has an out-of-plane deformation. The out-of-plane deformations of sensors with and without guard ring were respectively measured by using the optical interferometer (NT1100, Veeco Instruments Inc., USA). The measurement results in figure 7(b) show the out-of-plane deformations of the central proof mass for accelerometers with and without the guard ring at different heating temperatures. The results indicate that the out-of-plane deformation Δd_2 of the proof mass with the guard-ring design is only $0.10 \mu\text{m}$, as temperature increases from room temperature to $150 \text{ }^\circ\text{C}$; however, the deformation Δd_1 of the proof mass without the guard ring is $0.72 \mu\text{m}$. Hence, the guard-ring design significantly suppresses the unwanted out-of-plane deformation due to the temperature variation.

4.2. Temperature coefficients of zero-g offset (TCO) and sensitivity (TCS) tests

The measurement setup in figure 8(a) was established to evaluate the zero-g offset variation of accelerometer sensing signals at different ambient temperatures. The sample and a hot plate were mounted onto the rotation table (AC1120S, ACUTRONIC Inc., USA). The three sensing axes on the accelerometer were subjected to different loads (by gravity)

by varying the rotation angle θ of the table. For instance, the Z-axis was under the load of 1 g and 0 g as rotation angles were $\theta = 0^\circ$ and $\theta = 90^\circ$, respectively. Meanwhile, the ambient temperature of the packaged accelerometer was controlled by the hot plate. Firstly, the zero-g offsets for the three sensing axes of the accelerometer with guard ring were characterized as -0.85 mV (X-axis), -0.98 mV (Y-axis) and 0.77 mV (Z-axis) at room temperature ($25 \text{ }^\circ\text{C}$). In comparison, the zero-g offsets of the accelerometer without guard ring were -1.23 mV (X-axis), -1.17 mV (Y-axis) and 0.59 mV (Z-axis) at $25 \text{ }^\circ\text{C}$. Measurement results in figure 8(b) show the zero-g offset of three-axis accelerometers varying from room temperature ($25 \text{ }^\circ\text{C}$) to $125 \text{ }^\circ\text{C}$. As depicted in the vertical axis of figure 8(b), the normalized zero-g offset is determined as follows:

$$\text{Normalized zero-g offset} = \frac{V_{0g(T1)} - V_{0g(T0)}}{V_{1g(T0)} - V_{0g(T0)}} \times 100\%, \quad (1)$$

where $V_{0g(T0)}$ is the zero-g offset measured at room temperature ($25 \text{ }^\circ\text{C}$ in this case), $V_{0g(T1)}$ is the zero-g offset measured at temperature T1, $V_{1g(T0)}$ is the output signal of the sensor under 1 g load (specified by the rotation table) at room temperature. The temperature coefficient of the zero-g offset (TCO) for different sensing axes is determined from the slope of each curve in figure 8(b). Thus, the TCOs of the accelerometer without guard ring are $5.54\% \text{ g } ^\circ\text{C}^{-1}$ (X-axis), $2.12\% \text{ g } ^\circ\text{C}^{-1}$ (Y-axis) and $-14.72\% \text{ g } ^\circ\text{C}^{-1}$ (Z-axis). After adding the guard ring to the accelerometer, the TCOs are significantly decreased to $0.80\% \text{ g } ^\circ\text{C}^{-1}$ (X-axis), $0.55\% \text{ g } ^\circ\text{C}^{-1}$ (Y-axis) and $-2.56\% \text{ g } ^\circ\text{C}^{-1}$ (Z-axis). In short, the TCOs of the accelerometer can be reduced by a factor of 4 (in the Y-axis) to 7 (in the X-axis) by using the guard-ring design.

The measurement results in figure 8(c) show the sensitivity variations of accelerometers as the temperature

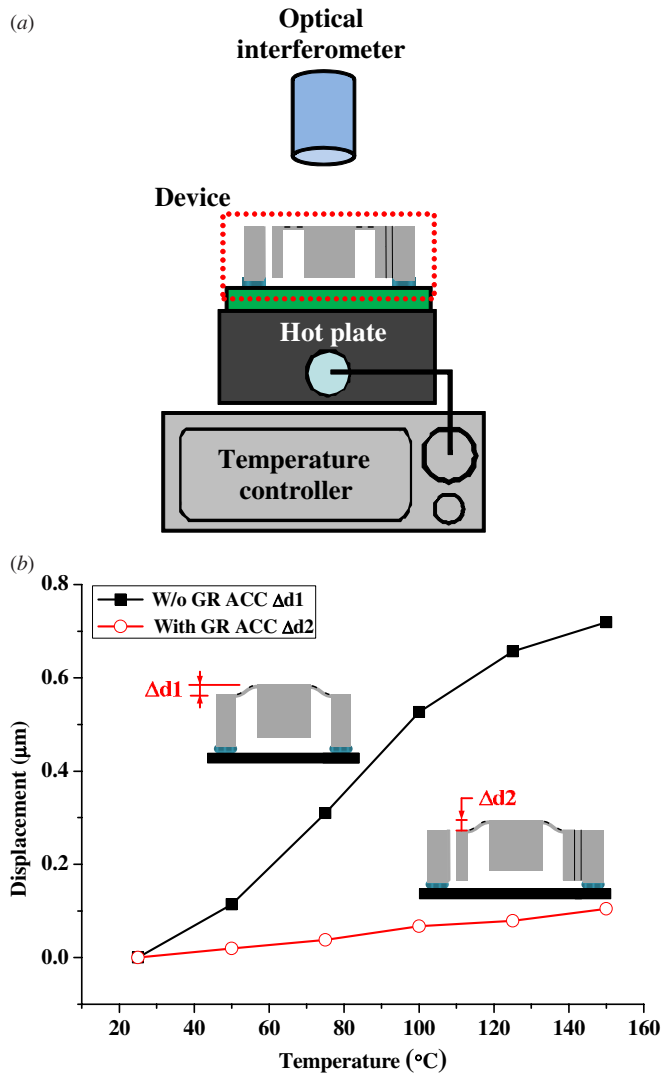


Figure 7. (a) Experimental apparatus for thermal deformation tests, (b) measurements of the out-of-plane spring deformations caused by temperature variations.

varies from room temperature (25 °C) to 125 °C. To determine the variation of sensitivity with temperature, the output voltage $V_{1g(T1)}$ of each sensing axis under 1 g load (specified by the rotation angle θ of the table) at temperature $T1$ is characterized. As depicted in the vertical axis of figure 8(c), the normalized sensitivity is determined as

$$\text{Normalized sensitivity} = \frac{(V_{1g(T1)} - V_{0g(T1)}) - (V_{1g(T0)} - V_{0g(T0)})}{V_{1g(T0)} - V_{0g(T0)}} \times 100\%. \quad (2)$$

The temperature coefficient of sensitivity (TCS) for different sensing axes is determined from the slope of each curve in figure 8(c). The TCSs of the present accelerometer are $-0.15\% \text{ g } ^\circ\text{C}^{-1}$ in the X-axis, $-0.14\% \text{ g } ^\circ\text{C}^{-1}$ in the Y-axis and $-0.16\% \text{ g } ^\circ\text{C}^{-1}$ in the Z-axis. The results also indicate that the TCS of the proposed accelerometer has less than 13% deviation. In comparison, the TCSs of the accelerometer without guard ring are $0.24\% \text{ g } ^\circ\text{C}^{-1}$ in the X-axis, $0.24\% \text{ g } ^\circ\text{C}^{-1}$ in the Y-axis and $1.77\% \text{ g } ^\circ\text{C}^{-1}$ in the Z-axis, and

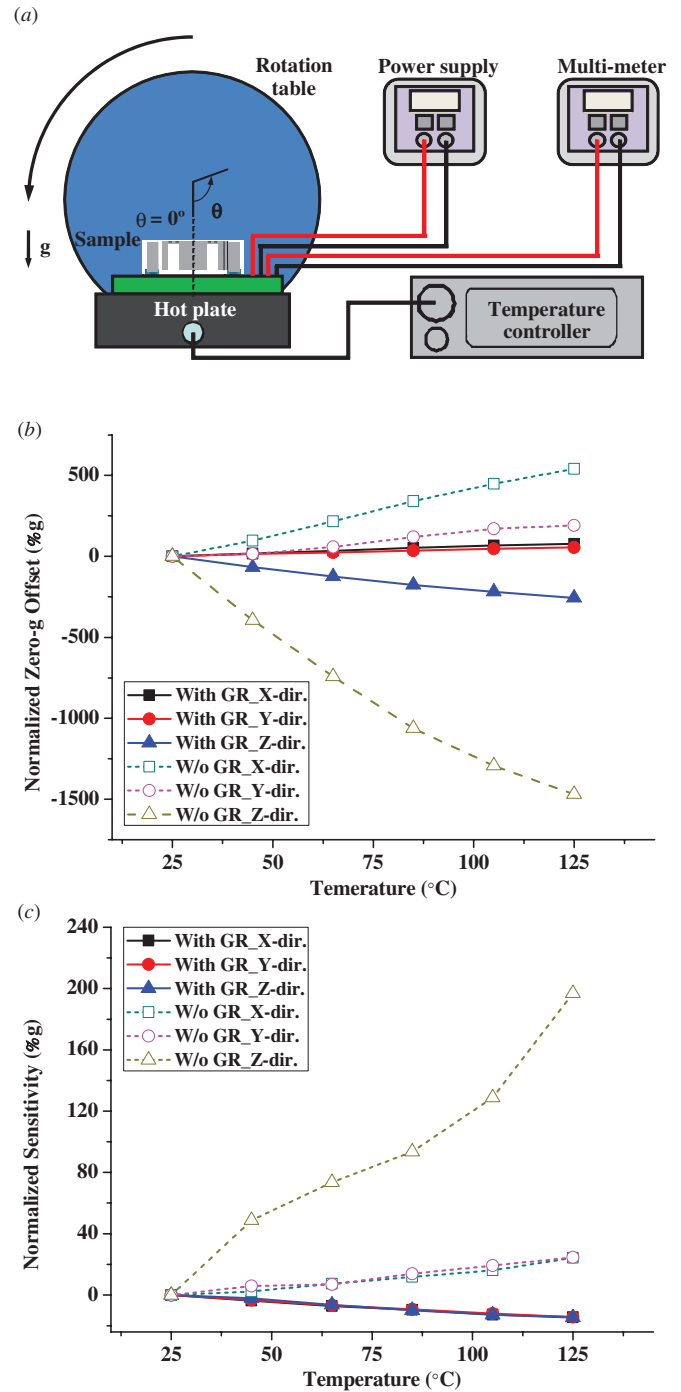


Figure 8. (a) Measurement setup for TCO and TCS tests, and (b), (c) the measurements of temperature-dependent zero-g offset and sensitivity of the accelerometers with and without guard ring.

its deviation is about 86%. Moreover, as ambient temperature changes, the sensitivity of the piezoresistive sensor will be influenced by the temperature coefficient of the piezoresistive coefficient and the thermal loads on piezoresistors [19]. As the temperature coefficient of the piezoresistive coefficient dominates the sensitivity variation, the TCS will be negative [20, 21]. The TCS becomes positive if thermal load is the major effect for sensitivity variation. Thus, the curve slopes

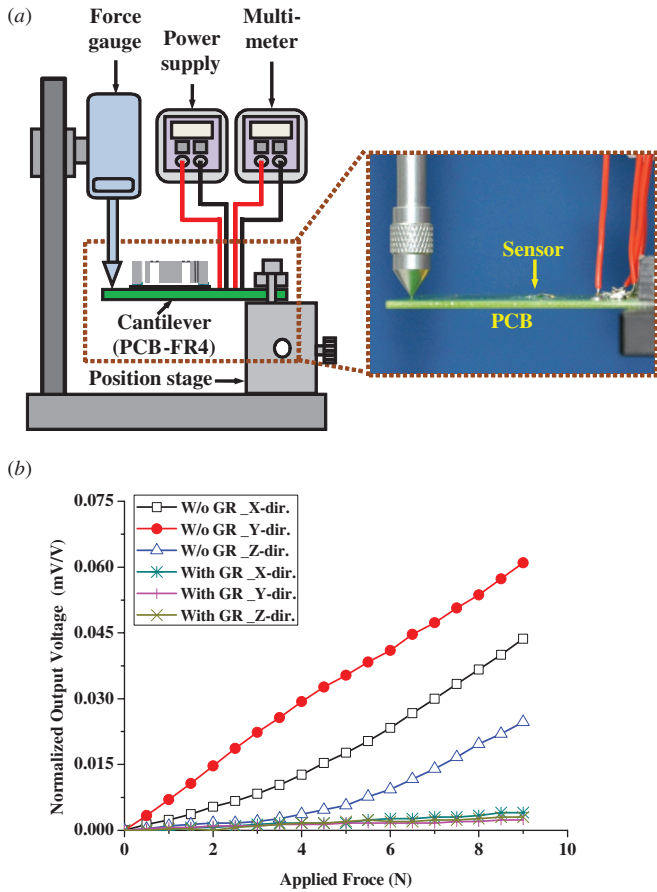


Figure 9. (a) Measurement setup for force/displacement transmittance tests, (b) results to show false signals induced by force/deflection transmittance from the substrate (PCB).

in figure 8(c) also indicate that the TCS of the accelerometer with guard ring successfully suppresses the thermal loads.

4.3. Force/displacement transmittance tests of the accelerometers

The experimental setup in figure 9(a) was established to evaluate the influence of the accelerometer as the unwanted force and deflection disturbances transmitted from the substrate. The accelerometer chip with the handling silicon layer was also adhered to the PCB. The force gauge with 1 mN resolution was used to apply load on the PCB. As the flexible PCB with one fixed end was bent by the applied load, a displacement would transmit from the PCB to the adhered chip, and caused a false signal output from the accelerometer. Such false output voltages of the accelerometer were recorded by the multimeter. Figure 9(b) shows the variation of output sensing voltages with the external applied force. The results indicate that the false signals induced by the forces and deflections transmitted from the PCB are significantly suppressed by the guard ring. In this experiment, the PCB has a bending curvature of 1.82 m caused by a 9 N external load, and the false signals were reduced by a factor of 8 (in the Z-axis) to 26 (in the Y-axis) by means of the guard-ring design.

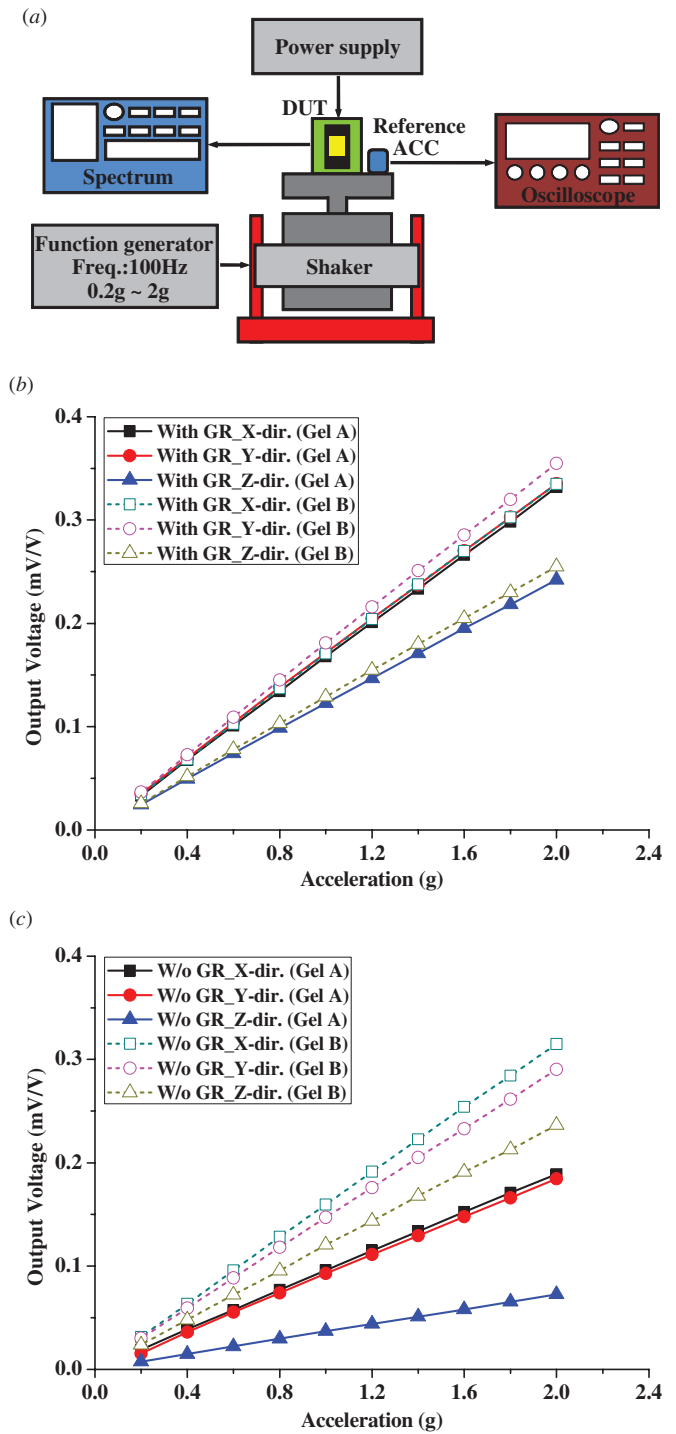


Figure 10. (a) Measurement setup to characterize the sensitivity and linearity of accelerometers, (b), (c) the measured characteristics of the accelerometers (with and without guard ring) with different interface adhesives (gel A and gel B).

4.4. Sensitivity and linearity tests of the accelerometers with different interface adhesives

Finally, the performances of the conventional and proposed three-axis accelerometers were also characterized using the setup in figure 10(a). The electromagnetic shaker (LDS V406, LDS Inc., Denmark) was used to provide a harmonic excitation specified by the function generator to excite the

Table 3. Comparison of the three-axis accelerometers with and without guard ring (note: the measurements are on the accelerometers adhered to the PCB using gel A).

Items	Accelerometer without guard ring			Accelerometer with guard ring			Unit
	X-axis	Y-axis	Z-axis	X-axis	Y-axis	Z-axis	
Chip size	2.1 × 2.3 × 0.4			2.1 × 2.3 × 0.4			mm ³
Acceleration range	2			2			g
Sensitivity	0.10	0.09	0.04	0.17	0.17	0.12	mV V ⁻¹ g ⁻¹
Nonlinearity	-0.82	-0.98	-0.25	-0.96	-1.02	-0.58	%
Zero-g offset (25 °C)	-1.23	-1.17	0.59	-0.85	-0.98	0.77	mV
Temperature coefficient of zero-g offset	5.54	2.12	-14.71	0.80	0.55	-2.56	% g °C ⁻¹
Temperature coefficient of sensitivity	0.24	0.24	1.77	-0.15	-0.14	-0.16	% g °C ⁻¹
Resonant frequency	1.70	1.83	3.00	1.57	1.59	2.33	kHz

accelerometers. The dynamic characteristic of the shaker was monitored by using a commercial accelerometer (352C44, PCB Inc., USA) and an oscilloscope. The output voltage from the sensor was recorded by the spectrum analyzer. Moreover, in order to demonstrate the capability of the proposed design, the accelerometers were adhered on the PCB via two different die attachment gels. One of the gels is silver paste ABLEBOND 84-1LMISR4 (gel A) from Ablestik UK Ltd with Young's modulus of 3.9 GPa and CTE of 40 ppm °C⁻¹, and the other gel is silicone gel RTV 3145 (gel B) from Dow Corning Corporation with the lower Young's modulus of 6.9 MPa and CTE of 260 ppm °C⁻¹. Measurement results in figure 10(b) show the typical output voltages of the three-axis accelerometer with guard ring as the excitation accelerations range from 0.2 g to 2 g. The typical sensitivities of the present accelerometer adhered to gel A are 0.17 mV V⁻¹ g⁻¹ in the X-axis, 0.17 mV V⁻¹ g⁻¹ in the Y-axis and 0.12 mV V⁻¹ g⁻¹ in the Z-axis. The accelerometer has a symmetric design in both x- and y-axes (including piezoresistors), and thus the accelerometers (with or without guard ring) have very similar sensitivity for x- and y-axes. Moreover, the nonlinearity of the proposed accelerometer is less than 1.02%. Figure 10(b) also indicates that the accelerometer performances have less than 8% deviation for different gels. In comparison, measurements in figure 10(c) show the performances of the accelerometer without guard ring under two different die attachment gels. The output voltages are significantly influenced (about 66% deviation in the Z-axis) by the gels for the accelerometer without guard ring. Table 3 summarizes the characteristics of the three-axis accelerometers with and without guard ring, and they are adhered on the PCB with gel A.

5. Conclusions

In this study, a three-axis piezoresistive accelerometer with a stress isolation guard-ring structure is designed and implemented. Thus, the environment disturbances (temperature variation and force/deflection transmittance) for such a packaged three-axis piezoresistive accelerometer are significantly reduced. Simulations and measurements indicate that the first three vibration modes of the proposed spring-mass system with guard ring meet the requirement of the three-axis accelerometer. The unwanted higher

modes are far from the first three modes. Therefore, the performance of the proposed three-axis accelerometer with the guard-ring design has less influence on the dynamics of the spring-mass and guard-ring structures. Thermal disturbance experimental results show that the unwanted deformation between the proposed sensors is only 0.10 μm at 150 °C. The temperature coefficient of the zero-g offset for the presented sensor is reduced by a factor of 4 (in the Y-axis) to 7 (in the X-axis) by using the guard-ring design. The undesired temperature-induced sensitivity variation is minimized (less than 13%). In addition, the external force/deflection transmittance experimental results show that false signals are reduced by a factor of 8 (in the Z-axis) to 26 (in the Y-axis) as the PCB has a bending curvature of 1.82 m caused by a 9 N external load. Moreover, the proposed three-axis accelerometer has the characteristics of sensitivities ranging from 0.12 to 0.17 mV V⁻¹ g⁻¹ and nonlinearity <1.02%. These measurement results demonstrate that the accelerometer with guard ring significantly suppresses the influences of environmental disturbances, yet its three-axis sensing capability remains similar to the one without guard ring. The major design consideration of the proposed device is the stiffness of the guard ring. A relatively large guard ring with high stiffness was designed and implemented in this study. Thus, the addition of guard ring did not affect the original performance of the accelerometer. However, it is also important to consider the size of the guard ring for cost issue. The optimization of the die size and guard-ring stiffness would be an important future work for this study.

Acknowledgment

The authors would like to thank Delta Electronics Inc. (Taiwan) for supporting part of the sensors related manufacturing and test facilities.

References

- [1] Beardmore G 1997 Packaging for microengineered devices. Lessons from the real world *Proc. of IEE Colloquium Assembly Connections Microsystems (London, UK, May 1997)* pp 2/1-2/8
- [2] Lee Y C, Parviz B A, Chiou J A and Chen S 2003 Packaging for microelectromechanical and nanoelectromechanical systems *IEEE Trans. Adv. Packag.* **26** 217-26

- [3] Li G and Tseng A A 2001 Low stress packaging of a micromachined accelerometer *IEEE Trans. Electron. Packag. Manuf.* **24** 18–25
- [4] Dickerson T and Ward M 1997 Low deformation and stress packaging of micromachined devices *Proc. IEE Colloquium Assembly Connections Microsystems (London, UK, 7 May 1997)* pp 7/1–7/3
- [5] Lou X, Shi J, Zhang W and Jin Y 2005 Study on the packaging technology for a high-G MEMS accelerometer *IEEE 2005 Electronics Packaging Technology Conf. (Singapore, Dec 2005)* pp 103–6
- [6] Walwadkar S and Cho J 2006 Evaluation of die stress in MEMS packaging: experimental and theoretical approaches *IEEE Trans. Compon. Packag. Technol.* **29** 735–42
- [7] Lacsamana E S, Navarro R M, Mena M G, Felton L E and Webster W A 2005 Very thin packaging of capped MEMS accelerometer device *IEEE 2005 Electronics Packaging Technology Conf. (Singapore, Dec 2005)* pp 98–102
- [8] Rogers T 1992 Considerations of anodic bonding for capacitive type silicon-glass sensor fabrication *J. Micromech. Microeng.* **2** 164–6
- [9] Rogers T and Kowal J 1995 Selection of glass, anodic bonding conditions and material compatibility for silicon-glass capacitive sensors *Sensors Actuators A* **46–47** 113–20
- [10] Takao H, Matsumoto Y, Seo H, Ishida M and Nakamura T 1996 Analysis and design considerations of three dimensional vector accelerometer using SOI structure for high temperature range *Sensors Actuators A* **55** 91–7
- [11] Plaza J A, Esteve J and Cane C 2000 Twin-mass accelerometer optimization to reduce the package stresses *Sensors Actuators A* **80** 199–207
- [12] Spiering V L, Bouwstra S and Fluitman J H J 1993 Realization of mechanical decoupling zones for package-stress reduction *Sensors Actuators A* **37–38** 800–4
- [13] Spiering V L, Bouwstra S and Ruun M E J S 1993 On-chip decoupling zone for package-stress reduction *Sensors Actuators A* **39** 149–57
- [14] Hsieh H S, Chang H C, Hu C F, C L Cheng and Fang W 2011 A novel stress isolation guard ring design for the improvement of three-axis piezoresistive accelerometer *IEEE Transducers' 11 (Beijing, China, June 2011)* pp 1412–5
- [15] Okada K 1992 Tri-axial piezoresistive accelerometer *Technical Digest of the 11th Sensor Symp.* pp 245–8
- [16] Takao H, Matsumoto Y, Seo H-D, Tanaka H, Ishida M and Nakamura T 1995 Three dimensional vector accelerometer using SOI structure for high temperature *IEEE Transducers '95 (Stockholm, Sweden, June 1995)* pp 683–6
- [17] Amarasinghe R, Dao D V, Toriyama T and Sugiyama S 2006 Simulation, fabrication and characterization of a three-axis piezoresistive accelerometer *Smart Mater. Struct.* **15** 1691–9
- [18] Dao D V, Okada S, Dau V T, Toriyama T and Sugiyama S 2004 Development of a 3-DOF silicon piezoresistive micro accelerometer *Proc. 2004 Int. Symp. on Micro-NanoMechatronics and Human Science (Nagoya, Japan, Oct 2004)* pp 271–6
- [19] Sze S M 1994 *Semiconductor Sensors* (New York: Wiley) pp 182–5
- [20] Kloeck B 1989 Design, fabrication and characterization of piezoresistive pressure sensors, including the study of electrochemical etch stop *PhD Dissertation* University of Neuchâtel, Switzerland pp 100–9
- [21] Kanda Y 1982 A graphical representation of the piezoresistance coefficients in silicon *IEEE Trans. Electron Devices* **29** 64–70